



# Arctic stratospheric ozone as a precursor of ENSO events since 2000s



Jae-Heung Park<sup>1</sup> ✉, Ja-Ho Koo<sup>2</sup> ✉, Jong-Seong Kug<sup>1,3</sup> ✉, Su-Jung Lee<sup>1</sup>, Mi-Kyung Sung<sup>4</sup>, Joowan Kim<sup>5</sup>, Eun-Chul Chang<sup>5</sup>, Young-Min Yang<sup>6,7,8</sup>, Sang Seo Park<sup>9</sup>, Kyung-Hwan Kwak<sup>10</sup>, Ji-Hoon Oh<sup>11</sup>, Hyung-Jeon Kang<sup>1</sup> & Soon-Il An<sup>2</sup>

Variability in Arctic stratospheric ozone (ASO) has significant implications for surface climate. Using observational reanalysis datasets and Ozone Monitoring Instrument data, we found that the springtime ASO variations since the 2000s can serve as a precursor to El Niño–Southern Oscillation in the subsequent winter. Springtime ASO variability has become pronounced, particularly over Eurasia, due to the asymmetric structure of the Arctic stratospheric polar vortex. With the return of solar radiation to the Arctic in spring, elevated ASO increases solar absorption over Eurasia, contributing to localized stratospheric heating. This heating induces an upper-tropospheric cyclonic circulation over Siberia, facilitating wave energy propagation toward the tropical Pacific. Consequently, upper-level easterly and low-level westerly wind anomalies emerge over the equatorial Pacific, favoring El Niño development (cf. La Niña for decreased ASO). These results highlight the importance of chemical–radiative–dynamical processes in the Arctic stratosphere for understanding tropospheric climate variability.

Stratospheric ozone plays two primary roles in the Earth system. First, it protects both plants and animals by absorbing harmful ultraviolet radiation, which can be detrimental to their health and survival<sup>1–4</sup>. Second, by absorbing solar radiation, it helps regulate large-scale atmospheric circulations<sup>5–8</sup>, which in turn influence global hydrological cycles<sup>9–11</sup>. That is, the influence of stratospheric ozone extends beyond ecosystems, affecting climate and weather patterns. In this context, the significant depletion of stratospheric ozone—primarily caused by the use of chlorofluorocarbons (CFCs)—has been a major concern and the focus of extensive research<sup>2,5,12–18</sup> since its first detection over Antarctica in 1984<sup>19,20</sup>, an event commonly referred to as the ozone hole.

For the Arctic, ozone depletion events have been reported since the mid-1990s<sup>21–25</sup>. Particularly, the recent Arctic stratospheric ozone (ASO) depletion that occurred in 2020<sup>26–29</sup> approached levels relatively close to those observed in the Antarctic ozone hole (~220DU), despite the generally higher background ozone concentrations in the Northern Hemisphere. However, both the intensity and frequency of ozone depletion in the Arctic

are typically lower and more irregular than in the Antarctic, resulting in substantial ASO variability. The difference between the two poles arises from the greater atmospheric variability in the Arctic, primarily associated with the stratospheric polar vortex (SPV)<sup>30</sup> and the Brewer–Dobson circulation (BDC)<sup>31</sup>.

The SPV and BDC are also thermodynamically interconnected<sup>32</sup>; that is, a strong (weak) SPV is generally associated with a weak (strong) BDC. A strong SPV inhibits air mixing into the vortex and reduces ozone transport from the tropics and the summer hemisphere to the Arctic via the BDC<sup>32</sup>. Furthermore, when the SPV strengthens, extremely cold temperatures (below 195 K) often develop, enhancing chemical ozone depletion due to increased concentrations of active chlorine and bromine on polar stratospheric clouds (PSCs). In short, ASO is more likely to be depleted when the SPV is strong and the BDC is weak, and vice versa.

The variability of ASO has been reported to influence surface climate and weather patterns, particularly during spring when solar radiation returns to the Arctic<sup>33–35</sup>. A previous study demonstrated that depleted

<sup>1</sup>School of Earth and Environmental Sciences, Seoul National University, Seoul, South Korea. <sup>2</sup>Department of Atmospheric Sciences, Yonsei University, Seoul, South Korea. <sup>3</sup>Interdisciplinary Program in Artificial Intelligence, Seoul National University, Seoul, South Korea. <sup>4</sup>Korea Institute of Science and Technology, Seoul, South Korea. <sup>5</sup>Department of Atmospheric Science, Kongju National University, Gongju, South Korea. <sup>6</sup>Department of Environment & Energy, Jeonbuk National University, Jeonju-si, Jeollabuk-do, Republic of Korea. <sup>7</sup>School of Civil, Environmental, Resources and Energy Engineering, Jeonbuk National University, Jeonju-si, Jeollabuk-do, Republic of Korea. <sup>8</sup>Soil Environment Research Center, Jeonbuk National University, Jeonju-si, Jeollabuk-do, Republic of Korea. <sup>9</sup>Department of Civil Urban Earth and Environmental Engineering, Ulsan National Institute of Science and Technology (UNIST), Ulsan, South Korea. <sup>10</sup>School of Natural Resources and Environmental Science, Kangwon National University, Chuncheon, South Korea. <sup>11</sup>Scripps Institution of Oceanography, University of California San Diego, La Jolla, CA, USA. ✉e-mail: [jhp11010@gmail.com](mailto:jhp11010@gmail.com); [zach45@yonsei.ac.kr](mailto:zach45@yonsei.ac.kr); [jskug@snu.ac.kr](mailto:jskug@snu.ac.kr)

springtime ASO contributed to Arctic sea ice reduction by increasing both sea ice export toward the Atlantic Ocean and surface net heat fluxes<sup>36</sup>. Additionally, extreme ASO depletion reduces upper-tropospheric stability, leading to an increase in high clouds. This increase in high clouds can amplify surface warming over the Siberian Arctic through a positive long-wave cloud radiative effect during boreal spring<sup>33</sup>. ASO variability also affects sea surface temperature (SST) anomalies in the North Pacific via atmospheric teleconnections<sup>37</sup>. Notably, Xie et al.<sup>38</sup> proposed that a decrease (increase) in springtime ASO leads to El Niño (La Niña) events with a lag of approximately 20 months, mediated by the North Pacific Oscillation and the Victoria mode (a.k.a., North Pacific Gyre Oscillation), based on the analysis of the reanalysis dataset from 1986 to 2015.

Meanwhile, significant changes in the characteristics of the SPV have been observed since the 2000s<sup>39,40</sup>, coinciding with Arctic climate changes<sup>41–43</sup>. The SPV has weakened due to factors such as Arctic sea ice loss<sup>44–46</sup> and increased snow cover<sup>47,48</sup>, and now tends to exhibit a more asymmetric structure<sup>46,49</sup>. This altered structure of the SPV is expected to influence the spatiotemporal distribution of ASO<sup>46,47,50</sup>. Then, in boreal spring, when solar radiation returns to the Arctic, the modified ASO distribution changes the absorption of solar radiation, potentially triggering weather and climate responses that differ from those observed in previous decades<sup>35</sup>. However, research on these feedback processes remains limited and warrants further investigation.

As noted earlier, a previous study<sup>38</sup> reported a negative correlation between ASO and ENSO through pathways in the North Pacific with a lag of approximately 20 months during 1986–2015. Based on the previous findings, the present study revisits the mechanism by which ASO influences the tropical Pacific, focusing on the post-2000s in the context of recent changes in the SPV. We analyzed two observational reanalysis datasets—ECMWF Reanalysis Version 5 (ERA5) for the main figures and Modern-Era Retrospective Analysis for Research and Applications, Version 2 (MERRA2) for the supplementary figures—as well as data from the Ozone Monitoring Instrument (OMI). The consistency across these datasets suggests that springtime ASO has the potential to act as a precursor to ENSO events in the following winter, with a lag of approximately 8 months, through atmospheric teleconnections extending across the Eurasian continent. We discuss the implications of these findings for understanding how the stratosphere influences the troposphere and contributes to the development of ENSO events in recent decades.

## Results

### An emerging connection between spring ASO and the following winter ENSO since 2000

To examine the decadal modulation of the ASO–ENSO relationship during 1980–2023, we conducted a 252-month running lead-lag correlation analysis between monthly ASO and ENSO indices. The monthly ASO index was obtained by averaging ozone concentrations over 70–90°N at 100–200 hPa (i.e., upper troposphere–lower stratosphere, UTLS). The Niño3.4 index (c.f., 120–170°W, 5°S–5°N) was adopted as the monthly ENSO index. For the ASO index, the UTLS altitude was selected, rather than higher altitudes where ozone concentrations are greater, as our focus was on climatic responses in the troposphere. However, we note that similar results were obtained even when the ASO index was calculated instead at a higher altitude (50–150 hPa), as shown in Supplementary Fig. 1. To highlight variability, both the climatological mean and linear trend were removed from the monthly ASO and ENSO indices within each 252-month running window, although this detrending had minimal effect on our results due to the small magnitude of the trend.

The results of the lead-lag correlation analysis are illustrated in Fig. 1a (refer to Supplementary Fig. 2 for MERRA2). On the x-axis, negative values indicate how many months ASO precedes ENSO, while positive values indicate how many months ENSO precedes ASO. Overall, correlations where ENSO precedes ASO are mostly positive but statistically insignificant throughout the analysis period. In contrast, correlations where ASO precedes ENSO undergo a marked change around the early 2000s. Before this

period, ASO preceded ENSO with a negative correlation at a lag of approximately 20 months, with the strongest signals occurring in the mid- to late 1990s. The negative correlation indicates that stratospheric conditions with increased ozone concentrations tended to precede La Niña about 20 months later, consistent with the findings of Xie et al.<sup>38</sup>. However, these negative ASO-preceding-ENSO signals gradually weakened over time, while positive ASO-preceding-ENSO signals with an 8-month lag emerged after the early 2000s.

The results in Fig. 1a reveal the emergence of a previously undocumented ASO–ENSO relationship since the early 2000s, characterized by elevated ozone concentrations preceding El Niño events in recent decades. To further investigate this lead-lagged relationship, we examined the lead-lag correlations between ASO and ENSO for the recent period (2002–2023), which corresponds to the second half of the full analysis period (1980–2023). Similar to Fig. 1a, the x-axis in Fig. 1b denotes how many months the ASO index precedes the ENSO index, while the y-axis indicates the calendar month of ASO from November (bottom) to October (top). The figure shows that ASO-preceding-ENSO signals are statistically significant when ASO in March–April precedes ENSO by 2–10 months. The highest correlation coefficient is 0.63 when ASO in April precedes ENSO in the following November. These results suggest that springtime ASO has consistently preceded ENSO events in the following winter since the early 2000s.

Based on Fig. 1b, we defined a March–April (MA) ASO index and a November–December (ND) ENSO index by averaging the monthly ASO and ENSO values over March–April and November–December, respectively. Figure 1c displays both the MA-ASO and ND-ENSO indices, which exhibit a correlation coefficient of 0.57, statistically significant at the 99% confidence level.

In addition to the reanalysis datasets, we utilized satellite-based ozone data from OMI/Aura Ozone (OMTO3; see “Methods”). Although OMTO3 provides total column ozone (TCO), rather than three-dimensional ozone fields and has a relatively short temporal coverage (2005–2023), TCO serves as a reliable proxy for stratospheric ozone because the highest number concentrations occur in the lower stratosphere (20–30 km). Following the same method applied to the ASO index, we derived an Arctic TCO index by averaging TCO over 70–90°N during March–April, after removing the climatological mean and linear trend (Fig. 1c). The correlation coefficient between MA-Arctic-TCO and MA-ASO indices is 0.79 (0.80 for MERRA2; Supplementary Fig. 2), significant at the 99% confidence level. Similarly, the correlation coefficient between the MA-Arctic TCO and the ND-ENSO indices is 0.52 (also 0.52 for MERRA2; Supplementary Fig. 2), significant at the 95% confidence level. These findings are consistent with the results from the reanalysis datasets, supporting the reliability of the observational reanalysis data since the 2000s.

### How does springtime ASO affect the development of ENSO in the following winter?

To investigate how springtime ASO is linked to the subsequent wintertime ENSO events since the early 2000s, we performed regression analyses of ozone concentration, air temperature, and wind anomalies at 200 hPa from February–March (FM) to June–July (JJ) (Fig. 2), and of wind anomalies at 850 hPa and SST anomalies from March–April (MA) to November–December (ND) (Fig. 3), onto the MA–ASO index (Supplementary Figs. 3 and 4 for MERRA2). Note that the results remain largely unchanged even when simultaneous ENSO-relevant signals are linearly removed from the ASO index using a regression method (Supplementary Fig. 5). This indicates that the findings are not artifacts of ENSO auto-correlation. Additionally, consistent results were obtained from a composite analysis based on events where the normalized ASO index exceeded 0.5 or fell below –0.5 (Supplementary Fig. 6).

In February–March (Fig. 2a), ozone concentrations are significantly elevated across the Arctic, with large-scale anomalous warming and circumpolar easterly wind anomalies. These results are indicative of a weakened SPV and a strengthened BDC. The strengthened BDC promotes

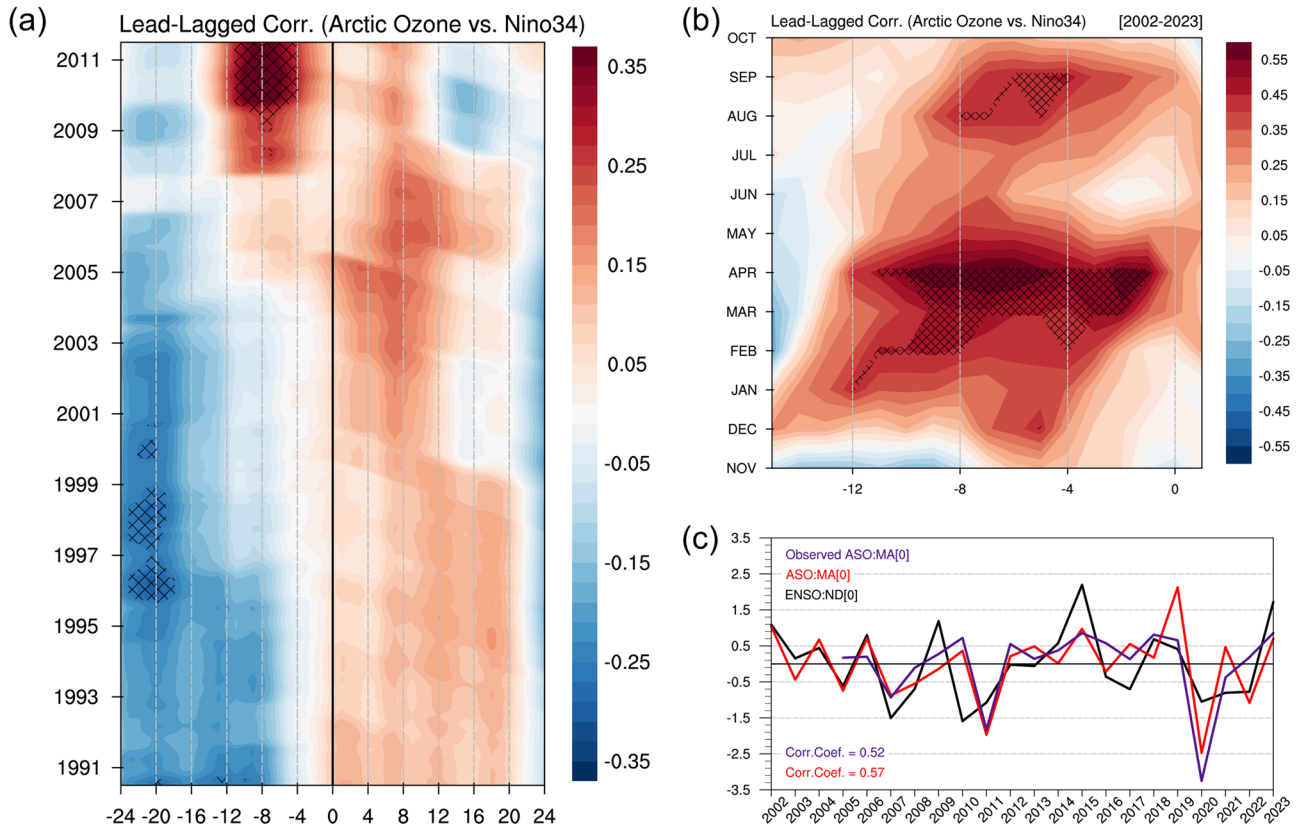


**Fig. 1 | Interdecadal modulation of the relationship between ASO and ENSO.** **a** 252-month (21-year) running lead-lagged correlation coefficients between the ASO and Niño3.4 indices for the period 1980–2023 (y-axis). Negative and positive values on the x-axis indicate leads of ASO and Niño3.4 at monthly timescales, respectively. Hatching denotes values significant at the 95% confidence level, based on a two-tailed Student’s *t*-test, with degrees of freedom set to 60 to account for temporal autocorrelation. **b** Lagged correlation between the ASO and Niño3.4 indices for the period 2002–2023, where the x-axis indicates the number of months by which the ASO index precedes the Niño-3.4 index; the y-axis indicates the period

of November to the following October. The negative maximum is found at 7 (x-axis) during April (y-axis), indicating that the ASO in April negatively precedes ENSO with a lag of 7 months. Hatching indicates the 95% confidence level using a two-tailed Student’s *t*-test (degree of freedom: 20). **c** Red and black lines indicate the March–April (MA) ASO index and the November–December (ND) Niño3.4 index from 2002–2023. The correlation coefficient between them is 0.57, significant at the 99% confidence level by student’s *t*-test (degree of freedom: 20). Herein, the purple line indicates the March–April (MA) Arctic total column ozone (TCO) index, obtained by averaging TCO over 70–90°N using OMI (2005–2023).

adiabatic warming and enhances ozone transport from the tropics to the Arctic. Simultaneously, the weakened SPV suppresses chemical ozone depletion. Herein, ozone transport by the BDC is expected to dominate over chemical loss processes, given the relatively high Arctic temperatures (mostly above 195 K), which inhibit the formation of polar stratospheric clouds (PSCs) (Supplementary Fig. 7). During this season, radiative heating from ozone absorption is minimal due to weak solar insolation (c.f., polar night). Thus, circulation-driven processes are likely the primary driver of the observed anomalies in February–March.

As the SPV weakens and contracts from winter to spring, significant easterly wind anomalies are confined to the high latitudes of Eurasia during March–April (Fig. 2b). Simultaneously, localized warming over these regions emerges, likely driven by subsidence associated with the BDC during the late-winter to early-spring transition and partly linked to the final stratospheric warming. Ozone concentrations remain elevated across the Arctic; however, the anomalies become increasingly concentrated over the Eurasian sector (~80 ppb at 60°N), in spatial alignment with the warming pattern. This elevated ozone concentration tilting toward the Eurasian continent becomes more pronounced at higher altitudes (~160 ppb at 150 hPa). The elevated ozone is inferred to enhance localized warming through increased absorption of solar radiation, as sunlight begins to return to the Arctic in spring following the polar night. Around this time, a cyclonic circulation anomaly begins to form south of the easterly wind anomalies and appears to propagate southeastward toward East Asia (see also Supplementary Figs. 3 and 5).

In April–May (Fig. 2c), as increased solar radiation reaches the high-latitudes, the upper-tropospheric cyclonic circulation anomaly over Siberia intensifies. This is accompanied by anomalous stratospheric warming (~1 °C) and enhanced ozone concentrations (~100 ppb). This localized warming is particularly pronounced at higher altitudes (e.g., 100–150 hPa), but is absent at lower levels (e.g., 300 hPa), suggesting that ozone-induced heating leads to vertical thermal expansion centered in the stratosphere (Supplementary Fig. 8). This vertical thermal expansion is expected to generate a dipolar response in circulation: a cyclonic anomaly below, associated with increased potential vorticity, and an anticyclonic anomaly aloft, associated with reduced potential vorticity.

Based on the above results, we further examined the baroclinic structure of the atmospheric circulation induced by ozone heating, focusing on the relationships among ozone, temperature at 150 hPa, and geopotential heights at 30 and 250 hPa over Siberia, where ozone concentrations are highest. We selected 150 hPa as the representative altitude for ozone, as it corresponds to the midpoint of the ASO index, which is defined by averaging ozone concentrations between 100 and 200 hPa. A scatter plot of ozone versus temperature at 150 hPa (Fig. 4a) shows a positive correlation, with a slope of approximately 1 °C per 100 ppb of ozone. We then examined how changes in ozone and temperature at 150 hPa affect upper- and lower-level geopotential heights. As ozone and temperature increase, the geopotential height at 30 hPa increases (Fig. 4b, c), whereas geopotential height at 250 hPa decreases (Fig. 4d, e). These results suggest that the upper-tropospheric cyclonic circulation anomaly over Siberia is attributable to ozone heating.

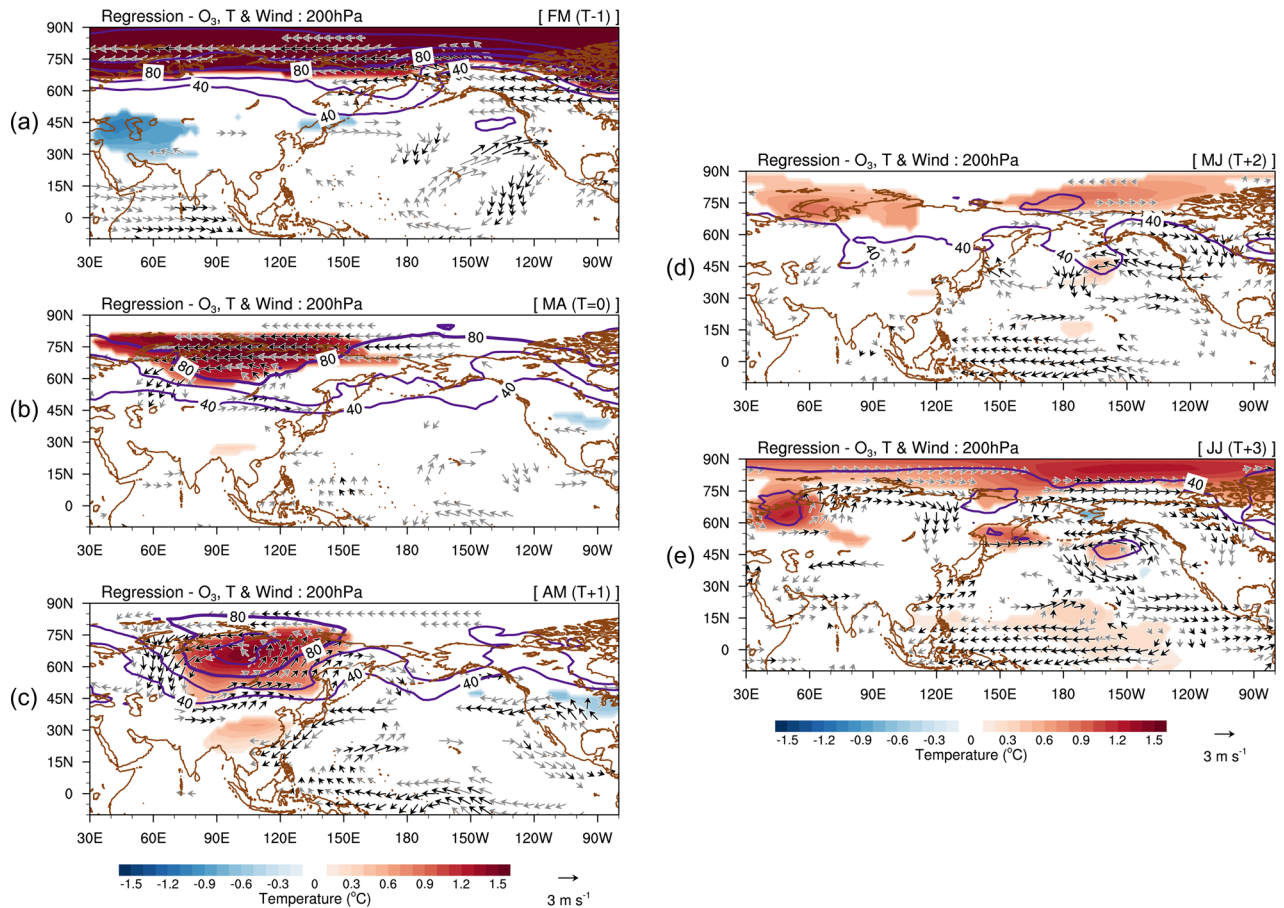


**Fig. 2 | Evolution of anomalous atmospheric variables at 200 hPa in terms of the springtime ASO.** **a** Regressed air temperature (shaded, °C; shading bar at bottom), ozone concentration (contour, interval: 20 ppbm), and wind anomaly (vector) at 200 hPa in February–March (t-1) against the springtime (March–April: t+0) ASO index for the period 2002–2023. Anomalous air temperature is marked as significant

at the 95% confidence level according to the Student’s *t*-test. For winds, areas satisfying the 95% and 85% confidence levels according to the Student’s *t*-test are marked in black and gray, respectively. **b–e** show similar figures to **(a)**, but for March–April (t+0), April–May (t+1), May–June (t+2), and June–July (t+3), respectively. For the Student’s *t*-test, the degrees of freedom were fixed at 20.

Notably, this springtime cyclonic circulation anomaly generates atmospheric waves that propagate southeastward, creating a sequence of anticyclonic, cyclonic, and anticyclonic circulations over East Asia, the western North Pacific, and the subtropical North Pacific, respectively (Fig. 2c). In other words, the wave train extends from Siberia to the tropical Pacific. As a result, upper-level easterly wind anomalies emerge along the western to central equatorial Pacific and persist into May–June and June–July (Fig. 2d, e). These upper-level easterly wind anomalies are expected to couple with the lower-level westerly wind anomalies, reflecting a baroclinic vertical structure over the equatorial Pacific<sup>51,52</sup>, which is conducive to the initiation of El Niño development.

Meanwhile, Fig. 3 illustrates SST and 850hPa wind anomalies from March–April through November–December, in association with the MA-ASO index. In March–April (Fig. 3a), easterly and northeasterly wind anomalies appear over the high latitudes of Eurasia and western Siberia. By April–May (Fig. 3b), these wind anomalies develop into a cyclonic anomaly over Siberia. This cyclonic circulation is accompanied by an anticyclonic anomaly over the Korea–Japan region and another cyclonic anomaly over the tropical western North Pacific, forming a wave-like pattern. These results suggest a tropospheric pathway linking the high latitudes of Eurasia to the tropical Pacific, with vertical coupling driven by upper-level circulations.

Over the tropical Pacific, low-level westerly wind anomalies begin to develop in the western tropical Pacific from March–April through May–June (Fig. 3a–c), accompanied by upper-level easterly wind anomalies. This vertical circulation connection is confirmed by the anomalous Walker

circulation pattern (Supplementary Fig. 9). Subsequently, these low-level westerly wind anomalies initiate anomalous SST warming along the equatorial Pacific through the Bjerknes feedback, driving the development of El Niño from spring through winter (Fig. 3d, e). Thus, these processes establish the observed 8-month lagged relationship between ASO and ENSO.

### The role of ASO-relevant forcing in modulating atmospheric circulation

We showed that stratospheric warming over Siberia associated with the ASO in spring accompanies an upper-tropospheric cyclonic circulation anomaly, which serves as a source of atmospheric waves propagating toward the tropical Pacific<sup>53,54</sup>. To examine how this upper-level cyclonic circulation over Siberia generates atmospheric waves extending toward the tropical Pacific, we employed the stationary wave model (SWM)—a simplified atmospheric general circulation model (Methods). In this experiment, the climatological mean atmospheric state during spring over 2002–2023 was used as the background atmospheric condition. Then, vorticity forcing over Siberia, resembling the upper-level cyclonic circulation anomaly in Fig. 2c, was imposed to assess its effect on the stationary wave response.

Figure 5a illustrates the horizontal and vertical structure of the prescribed atmospheric vorticity forcing, peaking at the 0.17 sigma level. Figure 5b shows the corresponding anomalous stationary atmospheric response at the same level. Notably, this response remains robust even when the horizontal or vertical placement of the vorticity forcing is slightly altered. In Fig. 5b, the atmospheric response exhibits a series of cyclonic and anticyclonic circulations over Siberia, the western North Pacific, the subtropical western

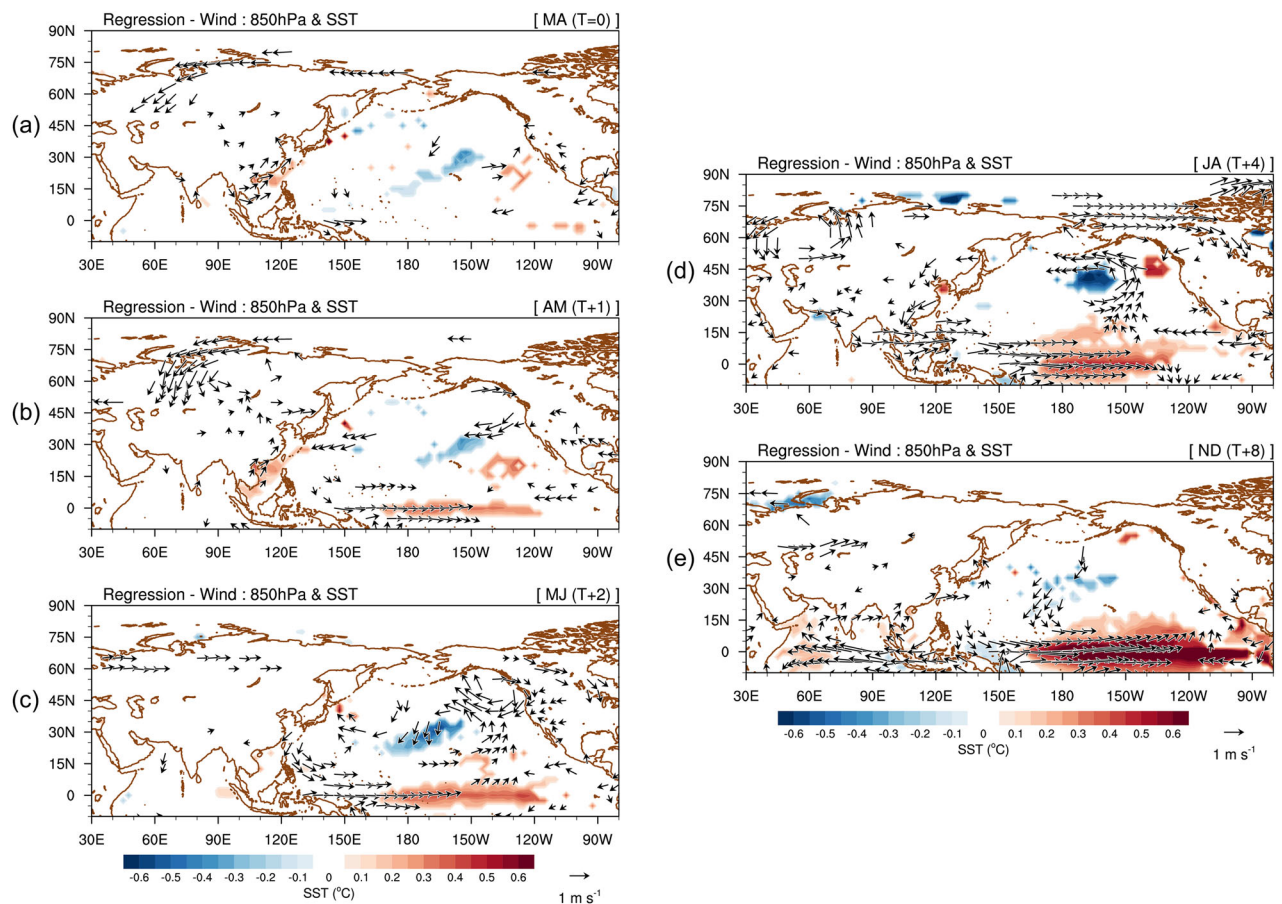


**Fig. 3 | Evolution of anomalous wind at 850 hPa and SSTA in terms of the springtime ASO.** **a** Regressed SSTA (shaded; °C, shading bar at bottom) and low-level wind anomaly (vector, at 850 hPa) in March–April ( $t + 0$ ) against the springtime (March–April) ASO index for the period 2002–2023. Anomalous SST

and winds are marked as significant at the 95% confidence level according to the Student’s  $t$ -test (degree of freedom: 20). **b–e** shows similar figures to **(a)**, but in April–May ( $t + 1$ ), May–June ( $t + 2$ ), July–August ( $t + 4$ ), and November–December ( $t + 8$ ), respectively.

North Pacific, and the tropical Pacific, under the background atmospheric state of April–May. A similar wave propagation pattern is also reproduced under the background atmospheric state of March–April (Supplementary Fig. 10). This stationary wave train closely resembles the observed atmospheric circulation anomalies regressed onto the MA-ASO index (Fig. 2c). Thus, these SWM experiment results suggest that ASO-induced vorticity forcing over Siberia can generate atmospheric waves propagating toward the tropical Pacific, potentially contributing to the onset of ENSO.

To diagnose the direction of wave propagation associated with upper-tropospheric cyclonic circulation over Siberia during spring (Fig. 2b, c), we analyzed the wave activity flux (WAF)<sup>35</sup> at 200 hPa for April–May (Fig. 5c; Supplementary Fig. 10 for March–April) under enhanced springtime ASO. The WAF analysis reveals that the wave activity propagates from Siberia, through East Asia, to the western North Pacific. Together, the results from the SWM experiment and WAF analysis underscore the key role of springtime ASO in modulating upper-tropospheric circulation via atmospheric wave responses to stratospheric heating.

### The role of SPV changes in the ASO–ENSO relationship

Figure 1a shows that the lagged ASO–ENSO relationship has undergone a noticeable change since the early 2000s. This shift coincides with prominent Arctic changes, such as a significant decline in sea ice extent (cf. polar amplification). Given these changes, it is essential to investigate how the climatological mean state changes have influenced the ASO–ENSO relationships. Previous studies have reported that the SPV has weakened since the 2000s, accompanied by an increase in Eurasian snow cover and enhanced vertical propagation of planetary waves<sup>47,48</sup>. Moreover, the SPV

has undergone structural changes, shifting from a symmetric and circular configuration to more asymmetric forms—such as a Eurasia-tilted or a split “peanut-shaped” structure—which have occurred more frequently in recent decades.

To investigate SPV changes after the 2000s, we analyzed 21 years of data divided into two periods: the first half period (1980–2001) and the second half period (2002–2023). Figure 6 shows the zonal wind, geopotential height, and temperature at 100 hPa for February–March and March–April, regressed onto the zonal wind index, which is defined by averaging the zonal wind at 100 hPa over 60–90°N in February (Supplementary Fig. 11 for MERRA2). These results capture SPV-related variability in zonal wind, GPH, and temperature in the mid-to-lower stratosphere. Note that similar patterns are also evident at higher altitudes where the SPV is climatologically strongest (Supplementary Fig. 12).

During 1980–2001 (Fig. 6a, b), the SPV remained strong and relatively symmetric in February–March, although it slightly weakened in March–April. In contrast, during 2002–2023 (Fig. 6c, d), the SPV preserved a symmetric structure in February–March, but became more asymmetric in March–April, exhibiting increased variability toward both Eurasia and North America. Notably, the tilt toward the Eurasian continent became more pronounced<sup>39,40</sup>, providing a favorable condition for strong ozone variability over this region compared to other regions (Supplementary Fig. 13). This altered ozone variability is, in turn, expected to exert distinct impacts on regional weather and climate patterns<sup>32</sup>.

In summary, the changes in SPV characteristics after the 2000s have created favorable conditions for enhanced springtime ozone variability over Eurasia. This enhanced variability, in turn, contributes to the generation of

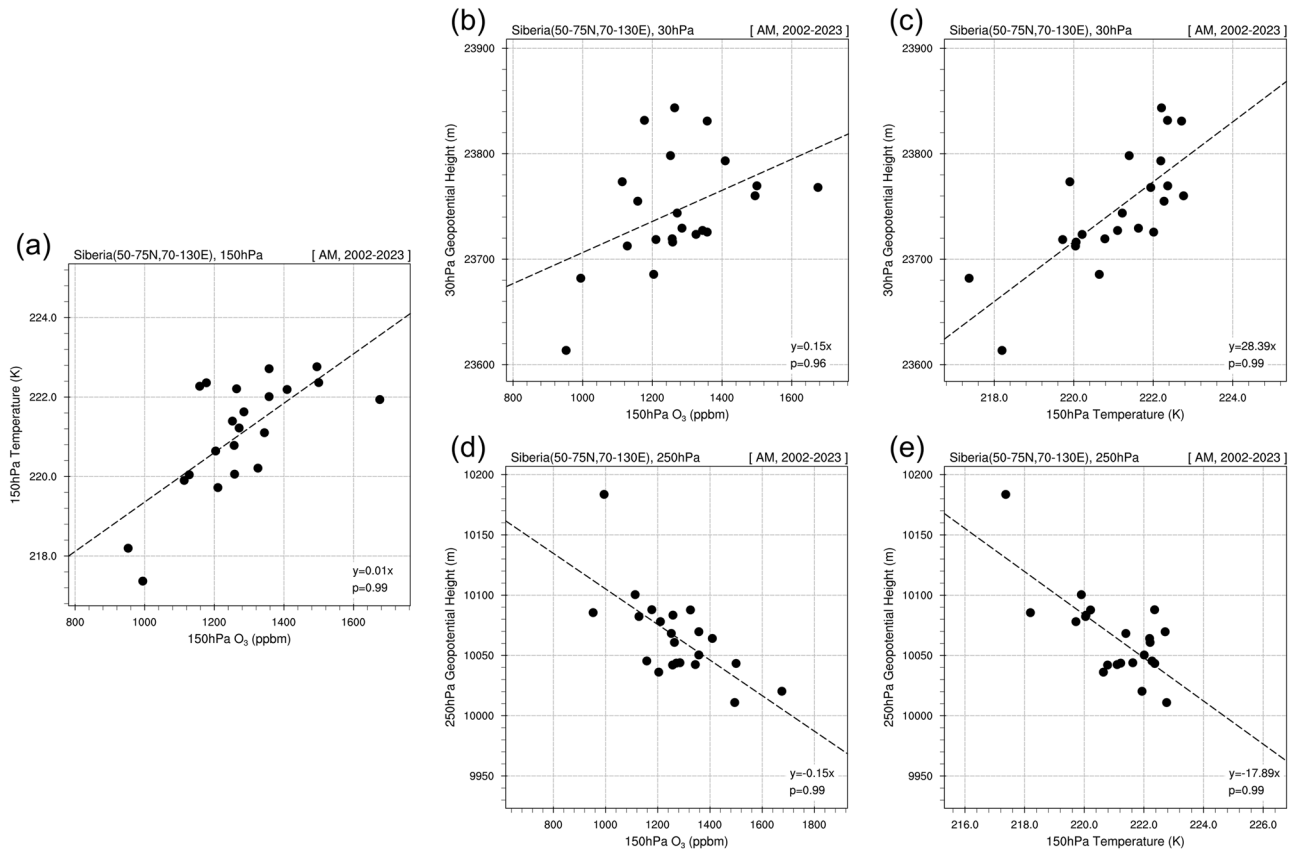
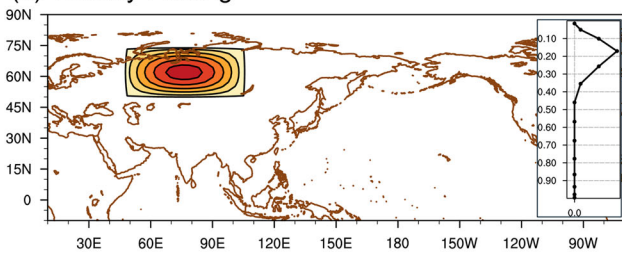


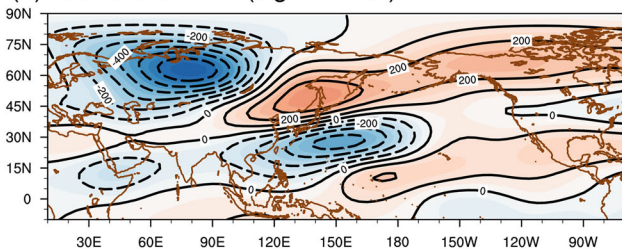
**Fig. 4 | Ozone-induced heating and its relationship with circulation.** Scatter plots of 150 hPa-ozone, 150 hPa-temperature, 250 hPa-GPH, and 30 hPa-GPH over Siberia (70–130°E, 50–70°N) during spring (March–April) 2002–2023. **a** 150 hPa-ozone and temperature. **b** 150 hPa-ozone and 30 hPa-GPH. **c** 150 hPa-temperature and 30 hPa-GPH. **d** 150 hPa-ozone and 250 hPa-GPH. **e** 150 hPa-temperature and 250 hPa-GPH.

SWM experiment (2002-2023, April-May)

(a) Vorticity Forcing



(b) Stream Function (sigma: 0.17)



(c) GPH-200hPa & Wave Activity Flux

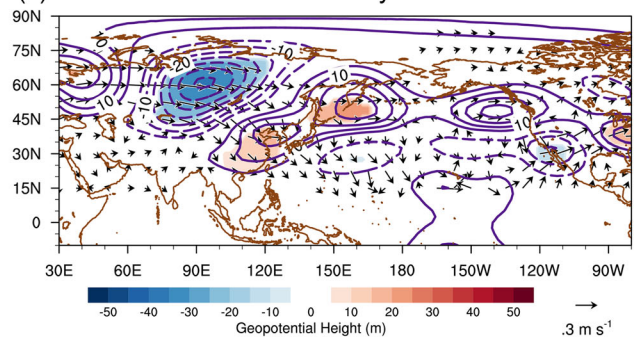


**Fig. 5 | Stationary wave model experiments with springtime ASO.** **a** Horizontal and vertical (inside panel) structure of steady vorticity forcing. **b** Steady response of atmospheric circulation (i.e., stream function) to the vorticity forcing in (a), under the April–May mean atmospheric state. **c** Geopotential height anomalies at 200 hPa

in April–May (shading, m) regressed on the ASO index and the relevant wave activity flux (vector) from ERA5, wherein wave activity flux over the low latitudes (<15°N) is conventionally masked out, due to the small Coriolis force.

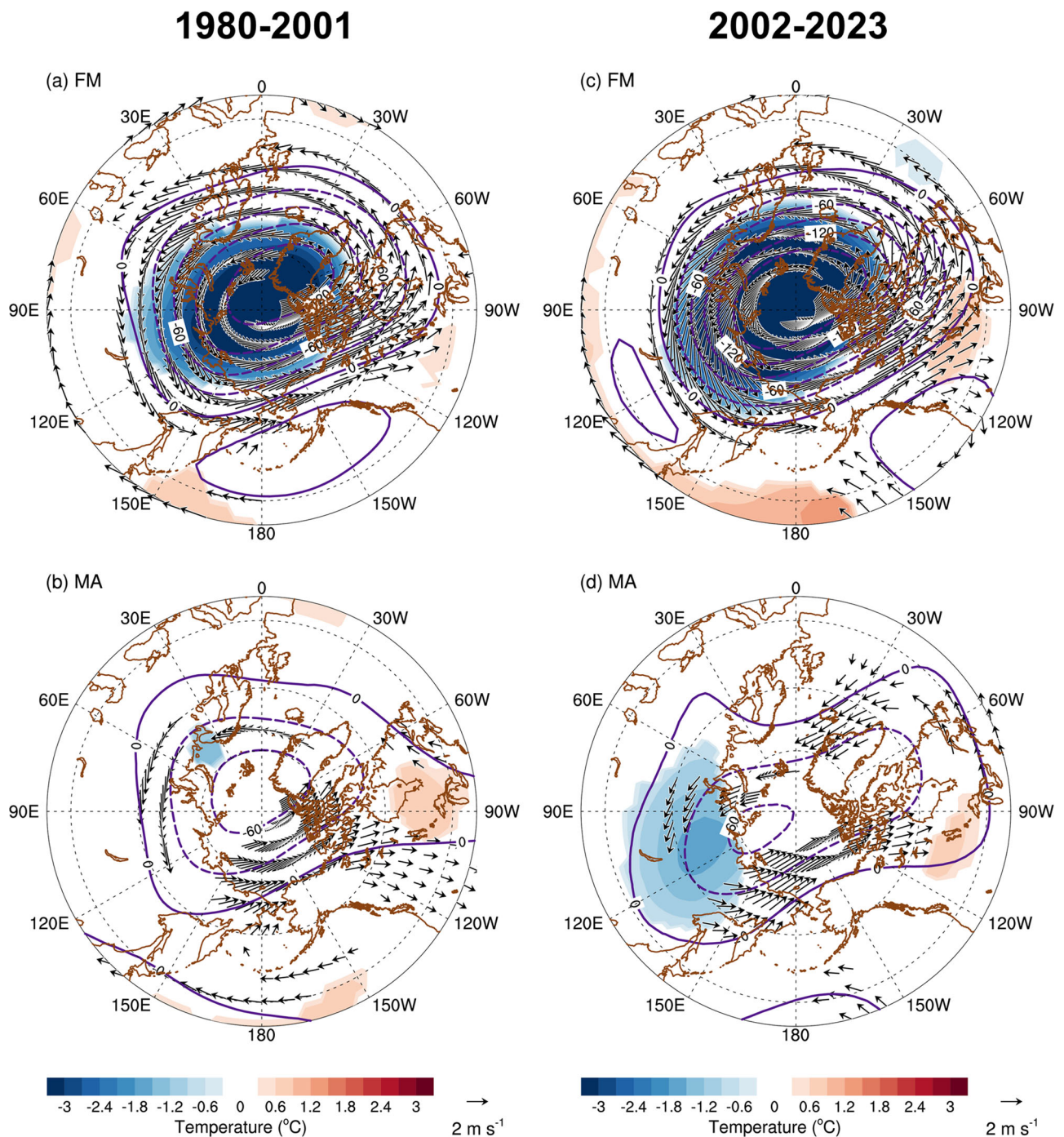


**Fig. 6 | Comparison between SPV variability between 1980–2001 and 2002–2023.** **a** Geopotential height (contour,  $m^2/s^2$ ), temperature (shading,  $^{\circ}C$ ), and wind (vectors,  $m/s$ ) anomalies at 100 hPa in February–March regressed onto the zonal wind

index (100 hPa, February; see manuscript) during 1980–2001. **b** Similar to (a), but for March–April. **c, d** are similar to (a, b), but for 2002–2023.

atmospheric waves propagating toward the tropical Pacific, thereby facilitating the emergence of the ASO–ENSO correlation observed in recent decades.

**Discussion**

A previous study by Xie et al.<sup>38</sup>, which analyzed observational reanalysis data from 1986 to 2015, identified a negative relationship between springtime ASO variability and the occurrence of ENSO events approximately 20 months later, through a North Pacific pathway. Building on these

findings, we revisited the ASO–ENSO relationship over the extended period of 1980–2023, during which substantial Arctic climate changes have occurred. Our analysis reveals a shift toward a positive ASO–ENSO relationship during 2002–2023, where increases (decreases) in ASO lead to the development of El Niño (La Niña) with an 8-month lag via a Eurasian pathway. We primarily attribute this shift to changes in the horizontal structure of ASO, shaped by altered characteristics of the SPV.

Since the characteristics of the SPV influence the horizontal distribution of ASO, it is reasonable to hypothesize a potential link between SPV

variability and subsequent ENSO events. However, our analysis indicates that ASO has a closer connection to ENSO than the SPV does (Supplementary Fig. 14). Additionally, when we defined a Siberian ozone index by averaging ozone concentration over Siberia (50–75°N, 70–130°E)—where ozone variability is pronounced (Fig. 2c)—and conducted a lead-lag correlation analysis similar to Fig. 1a, the relationship between Siberian ozone and ENSO exhibited similar decadal variations (Supplementary Fig. 15). These findings highlight the importance of considering the horizontal structure of ASO, in conjunction with SPV characteristics, for a better understanding of how stratospheric processes affect tropospheric atmospheric circulation.

Meanwhile, the ASO index in Fig. 1c appears to exhibit a biennial periodicity, which may be related to the influence of the Quasi-Biennial Oscillation (QBO), characterized by its typical cycle of 24–28 months<sup>56–58</sup>. To assess this potential influence, we removed the QBO signal from the ASO index using linear regression and re-evaluated the ASO–ENSO relationship. The results indicate that the relationship remains statistically significant even after accounting for the QBO influence, suggesting that the QBO has only a limited effect on the ASO–ENSO connection (Supplementary Fig. 16).

Chemistry–climate models project that the BDC will increase under global warming<sup>59–61</sup>, in which a weak and asymmetric structure of the SPV is expected. As long as the recent ASO–ENSO correlation seems to be connected to the weakening and asymmetric structure of the SPV and strengthened BDC, their relationship is expected to remain significant in future climates. Nonetheless, to gain deeper insight, it will be essential to compare historical data with global warming scenarios from various climate models, while considering the underlying chemical, radiative, and dynamic processes. This approach will be critical for understanding future climate variability and change.

Finally, our results in this study are mainly based on observational analysis with a relatively short period and a simple atmospheric general circulation model (SWM). That is, more discussion on the exact role of ASO in the climate system is necessary. Regarding this, further validation using coupled chemistry–climate models would be beneficial in the near future.

## Methods

### Stationary wave model (SWM)

The SWM is a nonlinear baroclinic model with a dry dynamical core and 14 vertical levels on sigma coordinates. Its horizontal resolution is truncated at rhomboidal 30. This model was devised to understand how atmospheric stationary waves propagate given atmospheric perturbations. To perform SWM experiments, the (mostly monthly or seasonal) background atmospheric state is first fixed. Then, under the fixed background state, steady atmospheric vorticity or heating forcings are prescribed until stationary atmospheric waves are obtained (mostly 30–60 days). The response to the forcing shown in Fig. 4 is averaged for 55 days, since the steady forcing is exerted. Further details of the model equations or information can be found in Ting and Yu<sup>62</sup> and Wang and Ting<sup>63</sup>.

### Data availability

Reanalysis datasets: we utilized the ECMWF Reanalysis v5 (ERA5)<sup>64</sup> and the Modern-Era Retrospective analysis for Research and Applications, version 2 (MERRA-2)<sup>65</sup>. ERA5 is the fifth generation of ECMWF reanalysis for global climate and weather for the past 4–7 decades, produced using 4D-Var data assimilation in CY41R2 of ECMWF's Integrated Forecast System (IFS), with 137 hybrid sigma/pressure levels in the vertical, with the top level at 0.01 hPa. MERRA2 is a global atmospheric reanalysis produced by the NASA Global Modeling and Assimilation Office (GMAO). It spans the satellite observing era from 1980 to the present. The goals of MERRA2 are to provide a regularly-gridded, homogeneous record of the global atmosphere, and to incorporate additional aspects of the climate system, including trace gas constituents (stratospheric ozone), and improved land surface representation, and cryospheric processes. MERRA2 is also the first satellite-era global reanalysis to assimilate space-based observations of aerosols and represent

their interactions with other physical processes in the climate system. In this study, the satellite ozone dataset is also utilized. The OMTO3e<sup>66</sup> dataset was selected, which is a Level-3 Aura/OMI product providing global gridded data of TOMS-like total column ozone (TCO). It features a spatial resolution of 0.25° latitude by 0.25° longitude. The OMTO3e product is generated by selecting the highest-quality level-2 total column ozone data (OMTO3) for each grid cell, prioritizing pixels with the shortest path length. Each OMTO3e file includes daily measurements of total column ozone, radiative cloud fraction, and solar and viewing zenith angles, derived from approximately 15 satellite orbits. The above datasets can be downloaded from open URLs: ERA5: <https://cds.climate.copernicus.eu/datasets>; MERRA2: [https://gmao.gsfc.nasa.gov/reanalysis/MERRA-2/data\\_access/](https://gmao.gsfc.nasa.gov/reanalysis/MERRA-2/data_access/); OMTO3: [https://disc.gsfc.nasa.gov/datasets/OMDOAO3e\\_003/summary](https://disc.gsfc.nasa.gov/datasets/OMDOAO3e_003/summary).

### Code availability

Codes used in the manuscript are available upon reasonable request from J.-H. Park (jhp11010@gmail.com).

Received: 15 April 2025; Accepted: 26 August 2025;

Published online: 06 October 2025

## References

- Slaper, H., Velders, G. J. M., Daniel, J. S., De Groot, F. R. & Van der Leun, J. C. Estimates of ozone depletion and skin cancer incidence to examine the Vienna Convention achievements. *Nature* **384**, 256–258 (1996).
- Solomon, S. Stratospheric ozone depletion: a review of concepts and history. *Rev. Geophys.* **37**, 275–316 (1999).
- Kerr, J. B. & McElroy, C. T. Evidence for large upward trends of ultraviolet-B radiation linked to ozone depletion. *Science* **262**, 1032–1034 (1993).
- Lubin, D. & Jensen, E. H. Effects of clouds and stratospheric ozone depletion on ultraviolet radiation trends. *Nature* **377**, 710–713 (1995).
- Thompson, D. W. J. et al. Signatures of the Antarctic ozone hole in Southern Hemisphere surface climate change. *Nat. Geosci.* **4**, 741–749 (2011).
- Son, S.-W. et al. The impact of stratospheric ozone recovery on the Southern Hemisphere westerly jet. *Science* **320**, 1486–1489 (2008).
- Gillett, N. P. & Thompson, D. W. J. Simulation of recent Southern Hemisphere climate change. *Science* **302**, 273–275 (2003).
- Polvani, L. M., Waugh, D. W., Correa, G. J. P. & Son, S.-W. Stratospheric ozone depletion: the main driver of twentieth-century atmospheric circulation changes in the Southern Hemisphere. *J. Clim.* **24**, 795–812 (2011).
- Kang, S. M., Polvani, L. M., Fyfe, J. C. & Sigmond, M. Impact of polar ozone depletion on subtropical precipitation. *Science* **332**, 951–954 (2011).
- Gonzalez, P. L. M., Polvani, L. M., Seager, R. & Correa, G. J. P. Stratospheric ozone depletion: a key driver of recent precipitation trends in South Eastern South America. *Clim. Dyn.* **42**, 1775–1792 (2014).
- Ma, X. et al. Effects of Arctic stratospheric ozone changes on spring precipitation in the northwestern United States. *Atmos. Chem. Phys.* **19**, 861–875 (2019).
- Solomon, S. The mystery of the Antarctic ozone “Hole”. *Rev. Geophys.* **26**, 131–148 (1988).
- Solomon, S. Progress towards a quantitative understanding of Antarctic ozone depletion. *Nature* **347**, 347–354 (1990).
- Stolarski, R. et al. Measured trends in stratospheric ozone. *Science* **256**, 342–349 (1992).
- Hartmann, D. L., Wallace, J. M., Limpasuvan, V., Thompson, D. W. J. & Holton, J. R. Can ozone depletion and global warming interact to produce rapid climate change? *Proc. Natl. Acad. Sci. USA* **97**, 1412–1417 (2000).
- Hartmann, D. L. The Antarctic ozone hole and the pattern effect on climate sensitivity. *Proc. Natl. Acad. Sci. USA* **119**, 1–5 (2022).

17. Stone, K. A., Solomon, S., Kinnison, D. E. & Mills, M. J. On recent large Antarctic ozone holes and ozone recovery metrics. *Geophys. Res. Lett.* **48**, e2021GL095232 (2021).
18. Jones, A. E. & Shanklin, J. D. Continued decline of total ozone over Halley, Antarctica, since 1985. *Nature* **376**, 409–411 (1995).
19. Farman, J. C., Gardiner, B. G. & Shanklin, J. D. Large losses of total ozone in Antarctica. *Nature* **315**, 207–210 (1985).
20. Chubachi, S. Preliminary result of ozone observations at Syowa Station from February 1982 to January 1983. *Mem. Natl. Inst. Polar Res. Ser. I* **34**, 13–19 (1984).
21. Rex, M. et al. Prolonged stratospheric ozone loss in the 1995–96 Arctic winter. *Nature* **389**, 835–838 (1997).
22. Müller, R. et al. Severe chemical ozone loss in the Arctic during the winter of 1995–96. *Nature* **389**, 709–712 (1997).
23. Newman, P. A., Gleason, J. F., McPeters, R. D. & Stolarski, R. S. Anomalous low ozone over the Arctic. *Geophys. Res. Lett.* **24**, 2689–2692 (1997).
24. Müller, R. et al. HALOE observations of the vertical structure of chemical ozone depletion in the Arctic Vortex during winter and early spring 1996–1997. *Geophys. Res. Lett.* **24**, 2717–2720 (1997).
25. Manney, G. L., Froidevaux, L., Santee, M. L., Zurek, R. W. & Waters, J. W. MLS observations of Arctic ozone loss in 1996–97. *Geophys. Res. Lett.* **24**, 2697–2700 (1997).
26. Hu, Y. The very unusual polar stratosphere in 2019–2020. *Sci. Bull.* **65**, 1775–1777 (2020).
27. Lawrence, Z. D. et al. The remarkably strong Arctic stratospheric polar vortex of Winter 2020: links to record-breaking Arctic oscillation and ozone loss. *J. Geophys. Res. Atmos.* **125**, 1–21 (2020).
28. Manney, G. L. et al. Record-low arctic stratospheric ozone in 2020: MLS observations of chemical processes and comparisons with previous extreme winters. *Geophys. Res. Lett.* **47**, e2020GL089063 (2020).
29. Dameris, M. et al. Record low ozone values over the Arctic in boreal spring 2020. *Atmos. Chem. Phys.* **21**, 617–633 (2021).
30. Chipperfield, M. P. & Jones, R. L. Relative influences of atmospheric chemistry and transport on Arctic ozone trends. *Nature* **400**, 551–554 (1999).
31. Butchart, N. The Brewer-Dobson circulation. *Rev. Geophys.* **52**, 157–184 (2014).
32. Weber, M. et al. The Brewer-Dobson circulation and total ozone from seasonal to decadal time scales. *Atmos. Chem. Phys.* **11**, 11221–11235 (2011).
33. Xia, Y. et al. Significant contribution of severe ozone loss to the Siberian-Arctic surface warming in spring 2020. *Geophys. Res. Lett.* **48**, e2021GL092509 (2021).
34. Wang, T. et al. Surface ocean current variations in the North Pacific related to Arctic stratospheric ozone. *Clim. Dyn.* **59**, 3087–3111 (2022).
35. Wang, T. et al. Decadal changes in the relationship between Arctic stratospheric ozone and sea surface temperatures in the North Pacific. *Atmos. Res.* **292**, 106870 (2023).
36. Zhang, J. et al. Responses of Arctic sea ice to stratospheric ozone depletion. *Sci. Bull.* **67**, 1182–1190 (2022).
37. Xie, F. et al. Variations in North Pacific sea surface temperature caused by Arctic stratospheric ozone anomalies. *Environ. Res. Lett.* **12**, 114023 (2017).
38. Xie, F. et al. A connection from Arctic stratospheric ozone to El Niño–Southern oscillation. *Environ. Res. Lett.* **11**, 124026 (2016).
39. Seviour, W. J. M. Weakening and shift of the Arctic stratospheric polar vortex: Internal variability or forced response? *Geophys. Res. Lett.* **44**, 3365–3373 (2017).
40. Nakamura, T. et al. A negative phase shift of the winter AO/NAO due to the recent Arctic sea-ice reduction in late autumn. *J. Geophys. Res. Atmos.* **120**, 3209–3227 (2015).
41. Screen, J. A. & Simmonds, I. The central role of diminishing sea ice in recent Arctic temperature amplification. *Nature* **464**, 1334–1337 (2010).
42. Rantanen, M. et al. The Arctic has warmed nearly four times faster than the globe since 1979. *Commun. Earth Environ.* **3**, 1–10 (2022).
43. Nghiem, S. V. et al. Rapid reduction of Arctic perennial sea ice. *Geophys. Res. Lett.* **34**, L19504 (2007).
44. Kim, B. M. et al. Weakening of the stratospheric polar vortex by Arctic sea-ice loss. *Nat. Commun.* **5**, 4646 (2014).
45. Liang, Y. C. et al. The weakening of the stratospheric polar vortex and the subsequent surface impacts as consequences to Arctic Sea ice loss. *J. Clim.* **37**, 309–333 (2024).
46. Curbelo, J., Chen, G. & Mechoso, C. R. Lagrangian Analysis of the Northern Stratospheric Polar Vortex Split in April 2020. *Geophys. Res. Lett.* **48**, e2021GL093874 (2021).
47. Wang, Q., Duan, A., Zhang, C., Peng, Y. & Xiao, C. A connection from Siberian snow cover to Arctic stratospheric ozone. *Atmos. Res.* **307**, 107507 (2024).
48. Zhang, J., Tian, W., Chipperfield, M. P., Xie, F. & Huang, J. Persistent shift of the Arctic polar vortex towards the Eurasian continent in recent decades. *Nat. Clim. Chang.* **6**, 1094–1099 (2016).
49. Manney, G. L. et al. Polar processing in a split vortex: Arctic ozone loss in early winter 2012/2013. *Atmos. Chem. Phys.* **15**, 5381–5403 (2015).
50. Zhang, J. et al. Stratospheric ozone loss over the Eurasian continent induced by the polar vortex shift. *Nat. Commun.* **9**, 1–8 (2018).
51. Zhao, J., Sung, M. K., Park, J. H., Luo, J. J. & Kug, J. S. Part I observational study on a new mechanism for North Pacific Oscillation influencing the tropics. *npj Clim. Atmos. Sci.* **6**, 15 (2023).
52. Zhao, J., Sung, M. K., Park, J. H., Luo, J. J. & Kug, J. S. Part II model support on a new mechanism for North Pacific Oscillation influence on ENSO. *npj Clim. Atmos. Sci.* **6**, 16 (2023).
53. Sardeshmukh, P. D. & Hoskins, B. J. The generation of global rotational flow by steady idealized tropical divergence. *J. Atmos. Sci.* **45**, 1228–1251 (1988).
54. Hoskins, B. J. & Karoly, D. J. The steady linear response of a spherical atmosphere to thermal and orographic forcing. *J. Atmos. Sci.* **38**, 1179–1196 (1981).
55. Takaya, K. & Nakamura, H. A formulation of a phase-independent wave-activity flux for stationary and migratory quasigeostrophic eddies on a zonally varying basic flow. *J. Atmos. Sci.* **58**, 608–627 (2001).
56. Holton, J. R. & Tan, H.-C. The influence of the equatorial quasi-biennial oscillation on the global circulation at 50 mb. *J. Atmos. Sci.* **37**, 2200–2208 (1980).
57. Holton, J. R. & Tan, H.-C. The quasi-biennial oscillation in the Northern Hemisphere lower stratosphere. *J. Meteorol. Soc. Jpn.* **60**, 140–148 (1982).
58. Anstey, J. A. & Shepherd, T. G. High-latitude influence of the quasi-biennial oscillation. *Q. J. R. Meteorol. Soc.* **140**, 1–21 (2014).
59. Butchart, N. et al. Chemistry-climate model simulations of twenty-first century stratospheric climate and circulation changes. *J. Clim.* **23**, 5349–5374 (2010).
60. Li, F., Austin, J. & Wilson, J. The strength of the Brewer-Dobson circulation in a changing climate: coupled chemistry-climate model simulations. *J. Clim.* **21**, 40–57 (2008).
61. Garcia, R. R. & Randel, W. J. Acceleration of the Brewer-Dobson circulation due to increases in greenhouse gases. *J. Atmos. Sci.* **65**, 2731–2739 (2008).
62. Ting, M. & Yu, L. Steady response to tropical heating in wavy linear and nonlinear baroclinic models. *J. Atmos. Sci.* **55**, 3565–3582 (1998).
63. Wang, H. & Ting, M. Seasonal cycle of the climatological stationary waves in the NCEP–NCAR reanalysis. *J. Atmos. Sci.* **56**, 3892–3919 (1999).

64. Hersbach, H. et al. The ERA5 global reanalysis. *Q. J. R. Meteorol. Soc.* **146**, 1999–2049 (2020).
65. Gelaro, R. et al. The modern-era retrospective analysis for research and applications, version 2 (MERRA-2). *J. Clim.* **30**, 5419–5454 (2017).
66. Levelt, P. F. et al. The ozone monitoring instrument. *IEEE Trans. Geosci. Remote Sens.* **44**, 1093–1101 (2006).

## Acknowledgements

J.-H. Park was supported by the National Research Foundation of Korea (NRF) grant funded by the Korean government (MSIT) (NRF-2023R1A2C1004083). J.-H. Park, J.-H. Koo, S. S. Park, and K.-H. Kwak were supported by the NRF grant funded by the Korean government (MSIT) (RS-2023-00219830). J.-S. Kug was supported by the NRF grant funded by the Korean government (NRF-2022R1A3B1077622), the Korea Meteorological Administration Research and Development Program under Grant (RS-2025-02222417), and the Institute of Information & communications Technology Planning & Evaluation (IITP) grant funded by the Korean government (MSIT) [NO.RS-2021-II211343, Artificial Intelligence Graduate School Program (Seoul National University)]. Y.-M. Yang was supported by the NRF grant funded by the Korean government (MSIT) (Grant No. RS-2024-00416848). J.-H. Oh was supported by Basic Science Research Program through the NRF funded by the Ministry of Education (RS-2025-02653909).

## Author contributions

J.-H. Park conceived the research and produced the initial results and manuscript with S.-J. Lee. J.-H. Koo, J.-S. Kug, and J. Kim further developed the research and refined the manuscript. All authors contributed to the discussion.

## Competing interests

The authors declare no competing interests.

## Additional information

**Supplementary information** The online version contains supplementary material available at <https://doi.org/10.1038/s41612-025-01220-8>.

**Correspondence** and requests for materials should be addressed to Jae-Heung Park, Ja-Ho Koo or Jong-Seong Kug.

**Reprints and permissions information** is available at <http://www.nature.com/reprints>

**Publisher's note** Springer Nature remains neutral with regard to jurisdictional claims in published maps and institutional affiliations.

**Open Access** This article is licensed under a Creative Commons Attribution 4.0 International License, which permits use, sharing, adaptation, distribution and reproduction in any medium or format, as long as you give appropriate credit to the original author(s) and the source, provide a link to the Creative Commons licence, and indicate if changes were made. The images or other third party material in this article are included in the article's Creative Commons licence, unless indicated otherwise in a credit line to the material. If material is not included in the article's Creative Commons licence and your intended use is not permitted by statutory regulation or exceeds the permitted use, you will need to obtain permission directly from the copyright holder. To view a copy of this licence, visit <http://creativecommons.org/licenses/by/4.0/>.

© The Author(s) 2025